Accepted Article Preview: Published ahead of advance online publication

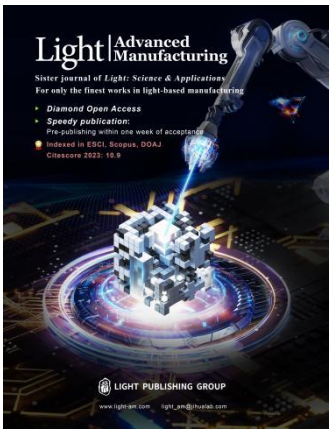

High Aspect-Ratio Meta-device for Broadband and High-Efficiency Terahertz Wave Manipulation

Zhiyan Zhu, Xiaotong Li, Junsuk Rho and Shulin Sun

Cite this article as: Zhiyan Zhu, Xiaotong Li, Junsuk Rho and Shulin Sun. High Aspect-Ratio Meta-device for Broadband and High-Efficiency Terahertz Wave Manipulation. *Light: Advanced Manufacturing* accepted article preview article preview 21 April, 2026; doi: 10.37188/lam.2026.070

Received 13 October 2025; revised 12 April 2026; accepted 19 April 2026; Accepted article preview online 21 April 2026

High Aspect-Ratio Meta-device for Broadband and High-Efficiency Terahertz Wave Manipulation

Zhiyan Zhu[1†], Xiaotong Li[2†], Junsuk Rho[2,3,4,5*] and Shulin Sun[1,6,7*]

[1] Shanghai Engineering Research Centre of Ultra Precision Optical Manufacturing, Department of Optical Science and Engineering, College of Future Information Technology, Fudan University, Shanghai, 200433, China

[2] Department of Mechanical Engineering, Pohang University of Science and Technology (POSTECH), Pohang, 37673, Republic of Korea

[3] Department of Chemical Engineering, Pohang University of Science and Technology (POSTECH), Pohang, 37673, Republic of Korea

[4] Department of Electrical Engineering, Pohang University of Science and Technology (POSTECH), Pohang, 37673, Republic of Korea

[5] POSCO-POSTECH-RIST Convergence Research Center for Flat Optics and Metaphotonics, Pohang, 37673, Republic of Korea

[6] Shanghai Key Laboratory of Metasurfaces for Light Manipulation, Shanghai, 200433, China

[7] Yiwu Research Institute of Fudan University, Yiwu, 322000, China

[*]Corresponding Authors: Junsuk Rho, E-mail: jsrho@postech.ac.kr

Shulin Sun, E-mail: sls@fudan.edu.cn

†These authors contributed equally to this work

ABSTRACT

Efficient terahertz (THz) wave manipulation is essential for advancing communications, imaging, and security detection. However, conventional THz devices based on natural materials suffer from the issues of bulky size, low efficiency, and narrow bandwidth. Although dielectric metasurfaces offer a promising alternative, their practical applications still face challenges in high-precision manufacturing, particularly for structures with high aspect-ratio (AR) and deep etching depth. Herein, we experimentally construct high-quality silicon meta-devices for THz wave-controls. Guided by the analysis of the potential structural imperfections, we propose an optimized fabrication method based on the Bosch etching technology to address these challenges and create silicon meta-atoms with high AR and vertical sidewall. As a proof-of-concept, we design and fabricate a half-wave plate (HWP) and a quarter-wave plate (QWP) with a maximum AR of 19.2:1 and broad working bands (0.6–0.8 THz and 0.5–0.8 THz). Their polarization conversion ratios (PCRs) can reach 0.915 and 0.99 at approximately 0.73 THz and 0.66 THz, respectively. Furthermore, we experimentally realize a highly efficient and broadband metalens exhibiting the high average focusing efficiency of 85.56% within 0.6–0.8 THz. Our fabrication methodology can be extended to fabricate other high-performance metasurfaces, opening new possibilities for broadband THz applications.

Keywords: dielectric metasurface, terahertz, Bosch process, polarization control, metalens

Introduction

Terahertz (THz) waves typically refer to electromagnetic (EM) waves covering a frequency spectrum from 0.1 to 10 THz, which is located at the interface regime between electronics and photonics[1, 2]. The novel EM properties, such as low photon energy, distinct fingerprint spectrum, and high penetrability, make THz technology highly applicable in next-generation wireless communications, security detection, medical diagnosis, and imaging[3-6]. Therefore, the manipulation of THz waves in the desired manner has emerged as an important topic in scientific researches and practical applications. Among numerous functional devices, the high-performance and ultra-compact platform capable of manipulating polarization states of THz waves are highly desired in various applications[7-9]. Unfortunately, conventional THz wave plates are usually of bulky sizes, low efficiencies and operate in a limited frequency band due to the weak interactions between natural materials and THz waves[10, 11].

In recent years, the rapid developments of metasurfaces have provided new opportunities for the realization of ultra-compact, small-footprint, and multifunctional devices working at different frequency regimes[12-16]. Specifically, metasurfaces are two-dimensional (2D) metamaterials constructed by planar microstructures (i.e., meta-atoms) with meticulously designed EM responses that are arranged in specific global sequences[17-20]. They have attracted considerable attention due to their strong capabilities to manipulate EM waves in subwavelength level. Many fascinating wave-manipulation effects have been realized, such as anomalous reflection/refraction[17, 18, 21, 22], surface wave excitation and manipulations[23-30], light beam focusing[31-35], specific- or multi- functional holographic imaging[36-42], complex beam generation[43-47], and so on. While metallic metasurfaces are widely utilized to tailor the wavefront of light waves through various resonance modes, they still face significant challenge of considerable intrinsic ohmic loss, which hinder their potential applications[48]. Recently, dielectric metasurfaces exhibit significantly lower absorption losses compared to the metallic counterparts, paving a new way for optical field manipulations[49-52].

While reviewing the advancements of all-dielectric meta-devices, we find that they usually encounter performance limitation in practical implementation[20, 53, 54]. Relying on the phase accumulation effect for light controls, the dielectric meta-atoms

usually require the high aspect-ratio (AR), implying that their practical fabrication necessitates the complicated deep etching technique[34, 55-57]. During this process, various fabrication imperfections, such as vertical etching depth error and lateral morphology error, commonly occur and negatively affect the performance of the device[58]. Therefore, it is crucial to develop an optimized deep-reactive-ion-etch (DRIE) technology for creating high-efficiency dielectric meta-devices in THz and other frequency regimes, which may significantly enhance their practical applications. In addition, dielectric meta-devices are often made by high-index dielectric materials, which may also experience significant reflection loss due to impedance mismatch issue[55, 59, 60].

In this work, we theoretically design and experimentally demonstrate transmissive dielectric metasurfaces for achieving high-efficiency and broadband THz wave manipulations, as schematically shown in Fig. 1a. Based on the Bosch etching technology [see Fig. 1c], we successfully construct the high-resistance lossless silicon pillar meta-atoms with high AR (about 19.2:1), yielding high transmission efficiency and full range of phase modulations. As a proof-of-concept, we create two THz meta-polarizers, including a half-wave plate (HWP) for achieving linear-linear polarization conversion and a quarter-wave plate (QWP) for achieving linear-circular polarization conversion. We numerically demonstrate that the vertical etching depth and lateral morphology significantly affect the performance of the meta-devices. Therefore, we propose an optimized fabrication methodology to develop high-quality silicon meta-devices. Experimental measurements indicate that the fabricated meta-HWP and meta-QWP possess high polarization conversion ratios (PCRs) of 0.6 within 0.6–0.8 THz (relative bandwidth: 28.57%) and 0.5–0.8 THz (relative bandwidth: 46.15%). The highest PCRs measured can reach 0.915 and 0.99 at approximately 0.73 THz and 0.66 THz, respectively. All experimental results are highly consistent with the full-wave simulations, confirming the effectiveness of the proposed fabrication methodology. Finally, we construct a Pancharatnam-Berry (PB) typed metalens with a high numerical aperture (NA) of 0.8 at 0.7 THz based on the proposed high-performance HWP meta-atoms, and experimentally verify that the average focusing efficiency can be well maintained at about 85.56% in the range of 0.6–0.8 THz.

Results

Generic principle of designing meta-atoms

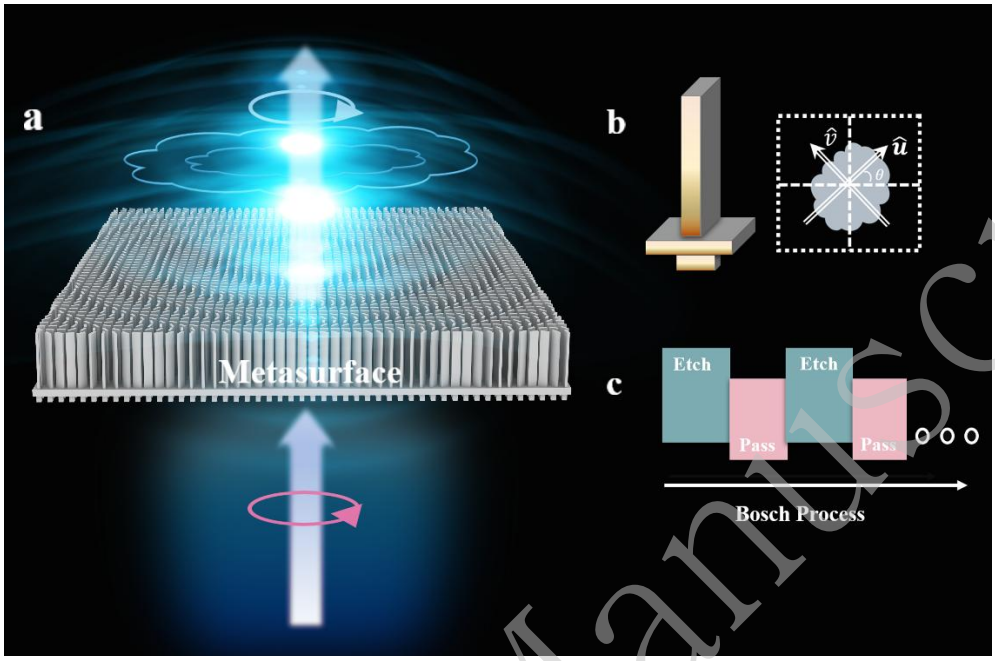

Fig. 1 Realization of dielectric meta-devices for achieving high efficiency wave manipulations. **a** Schematic of the high-efficiency wave-controls by the proposed dielectric meta-devices. **b** Schematic of the adopted high aspect-ratio (AR) dielectric meta-atom satisfying the mirror system along two principal axes *u* and *v*. **c** Schematic of the deep-reactive-ion-etch technique to fabricate the high AR meta-atom depicted in **b**.

We first introduce the theoretical design of the desired THz meta-devices as shown in Fig. 1. All proposed devices are constructed by the silicon meta-atom satisfying the mirror system as shown in Fig. 1b, whose transmission and reflection properties can be described by diagonal Jones matrices $\mathbf{T}(\mathbf{0}) = \begin{pmatrix} t_{uu} & 0 \\ 0 & t_{vv} \end{pmatrix}$ and $\mathbf{R}(\mathbf{0}) = \begin{pmatrix} r_{uu} & 0 \\ 0 & r_{vv} \end{pmatrix}$. Here, t_{uu}, t_{vv} and r_{uu}, r_{vv} denote the co-polarized transmission and reflection coefficients of the proposed meta-atoms under the excitation of the EM waves linearly polarized along the two principal axes (i.e., *u* and *v*), respectively. To achieve high-efficiency light manipulation, the desired meta-atoms designed in the transmission configuration should be highly transparent (i.e., $|t_{uu}| = |t_{vv}| = 1$, $|r_{uu}| = |r_{vv}| = 0$). While the meta-atoms are rotated by an

angle of θ (defined as the angle between the u axis of the meta-atom's local coordinate system and the x axis of the laboratory coordinate system) as shown in Fig. 1b, the Jones matrix of the meta-device can be expressed as $\mathbf{T}(\theta) = \mathbf{S}^{-1}(\theta)\mathbf{T}(\mathbf{0})\mathbf{S}(\theta)$, where $\mathbf{S}(\theta) = \begin{pmatrix} \cos\theta & \sin\theta \\ -\sin\theta & \cos\theta \end{pmatrix}$ is the transformation matrix connecting the local coordinate system and the laboratory coordinate system.

Utilizing the Jones matrix analysis, we can derive the theoretical criterion to design the high-performance meta-HWP satisfying the mirror symmetry (see more details in S1 of the Supplemental Material):

$$\begin{cases} |t_{uu}| = |t_{vv}| = 1 \\ \Delta\phi = \arg(t_{uu}) - \arg(t_{vv}) = \pi \\ \theta = \dfrac{\pi}{4} \end{cases} \tag{1}$$

Equation (1) indicates that the desired meta-HWP should be totally transparent along two principal axes and possess the phase difference of π for two cross linear polarization (LP) cases. All meta-atoms of the meta-device should have the identical orientation angle of $\theta = \pi/4$. For the design of meta-QWP, the following conditions can be simply derived as (see more details in S1 of the Supplemental Material):

$$\begin{cases} |t_{uu}| = |t_{vv}| = 1 \\ \Delta\phi = \arg(t_{uu}) - \arg(t_{vv}) = \dfrac{\pi}{2} \\ \theta = \dfrac{\pi}{4} \end{cases} \tag{2}$$

Equation (2) implies that the desired meta-QWP should be totally transparent along two principal axes and possess the phase difference of π/2 for two cross LP cases. The orientation angle of all the meta-atoms on the meta-device should be π/4. In addition, while the phase difference $\Delta\phi$ is equal to -π/2, the meta-device can realize another kind of LP-CP conversion.

Design of the high-performance silicon meta-atom

We now adopt the proposed strategy to construct the meta-atoms for creating the high-performance transmission-type meta-devices working in the THz regime. As

shown in Fig. 2a, the proposed building block consists of an amorphous silicon rectangular pillar with a high AR as the top layer, a continuous silicon spacer in the middle, and a square silicon microstructure as the bottom layer. Here, the high rectangular silicon pillar can offer a large phase difference ($\Delta\phi$) by means of the accumulated anisotropic transmission phases for the input THz waves of different LPs. Meanwhile, while amorphous silicon is almost lossless in the THz regime, such pillar structures possess the limited effective mode index, thus giving rise to the high transparency property. To address the large impedance mismatch issue between the silicon spacer and the air, the square-shape silicon microstructure is introduced as the anti-reflection layer. Since the effective index (or impedance) of the anti-reflection layer locates between the values of the air and bulky silicon, the reflection loss can thus be significantly suppressed. In our design, both the width and thickness of the anti-reflection layer have been carefully optimized to ensure the high transparency performance across the working band of the meta-device. In short, by fully optimizing the structural parameters, we can obtain the transmissive meta-atoms with high transmission efficiency and the arbitrary tailored $\Delta\phi$.

To clarify the working mechanism of the meta-atoms, we start to explore the optical responses of the simplified structures, i.e., the free-standing rectangular silicon ($n_{\mathrm{si}} = 3.35$) pillars. For the normal incident beams carrying different LPs ($\mathbf{E}||\hat{u}$ and $\mathbf{E}||\hat{v}$), we investigate how the transmission characteristics of such periodic meta-atoms vary against the lateral sizes (l and w). Here, the period (p) and the height (h_1) of the high AR silicon pillars are fixed as 125 and 480 μm, respectively. Full-wave simulation results demonstrate that the high AR meta-atoms can provide sufficient phase difference $\Delta\phi$ while maintaining high transmittances (See more details in S2 of the Supplemental Material). This clearly confirms that the proposed framework offers a broad design space capable of meeting the requirements of diverse polarization controls. Additionally, compared to the low AR counterparts, the high AR dielectric meta-atoms demonstrate larger phase retardation accumulated along the propagation direction, enabling more deeply subwavelength lateral dimension. This

characteristic offers substantial advantages for creating the various functional meta-devices.

After understanding the role played by the high AR silicon pillars, we next introduce the complete design of the dielectric meta-atoms utilized in practical applications. In the fabrication process, the high AR silicon pillar needs to lay on a flat silicon spacer as the supporting layer. However, since the refraction index of silicon is quite high, an additional silicon microstructure is designed at the bottom of the silicon spacer. This microstructure helps reduce the reflection loss of the whole meta-atom and is therefore called as the anti-reflection layer. Through numerical optimization, we have determined the following parameters for the desired anti-reflection layer: $h_3 = 62$ μm and $w_2 = 56$ μm (See more details in S3 of the Supplemental Material). It should be noted that, since the microstructure of the anti-reflection layer is isotropic, it does not contribute to the transmission phase difference $\Delta\phi$ accumulated inside the whole device.

After obtaining all basic parameters of the three layers, we calculate the co-polarization transmittance (T_{uu} and T_{vv}) and transmission phase difference ($\Delta\phi$) of such high AR silicon meta-atoms as functions of two key modulation parameters (i.e., l and w), as shown in Figs. 2b-d. All these results are obtained through finite-difference-time-domain (FDTD) simulations using Eastwave software. In our simulation setup, periodic boundary conditions are implemented around a single unit structure to effectively model an infinite periodic metasurface. One port is positioned 200 μm below the anti-reflection layer to emit the source wave, and another port is placed 200 μm above the silicon pillar to collect the transmission signal. Both the amplitude and phase of the transmission and reflection mode can be obtained through these two ports. Based on the phase diagram of design parameters, we can easily determine the optimal parameters for the high-performance HWP ($l = 100$ μm, $w = 30$ μm) and QWP ($l = 81$ μm, $w = 56$ μm) denoted as red and blue stars in Fig. 2b, respectively. We can see that the meta-atoms can serve as the ideal high-efficiency elements to tailor the polarization of input THz waves. Finally, to quantitatively evaluate the performance of the created HWP and QWP, we can define their PCRs as:

$$\mathrm{PCR_{HWP}} = \frac{1}{4}|t_{uu} - t_{vv}|^2$$
$$\mathrm{PCR_{QWP}} = \left|\frac{e^{-i\cdot\frac{\pi}{4}\cdot\left(t_{uu}\cdot\cos\left(\frac{\pi}{4}\right)+i\cdot t_{vv}\cdot\sin\left(\frac{\pi}{4}\right)\right)}}{\sqrt{2}}\right|^2 \quad (3)$$

Full-wave simulation results show that the inclusion of the anti-reflection layer not only broadens the working bandwidth but also significantly enhances the polarization conversion efficiency compared to the case without the anti-reflection layer (See more details in S4 of the Supplemental Material).

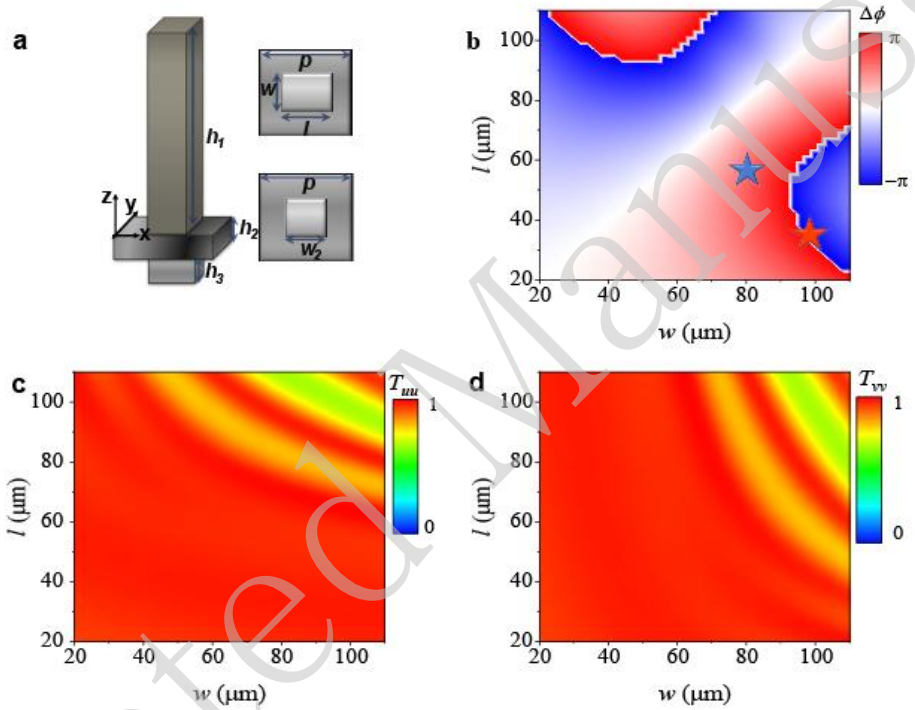

Fig. 2 Design of the proposed silicon meta-atom. **a** Schematic of silicon meta-atom consisting of high AR pillar (top), thin silicon spacer (middle) and an anti-reflection layer (bottom). **b-d** Simulated transmission phase difference ($\Delta\phi = \arg(t_{uu}) - \arg(t_{vv})$) and transmission efficiency (T_{uu} and T_{vv}) of the silicon meta-atom arranged in periodic arrays with different l and w at the frequency of 0.7 THz.

Impact of structural imperfection commonly existing in practical manufacturing on device performance

We now analyze the main manufacturing errors that will result in the performance deterioration, which is an important guidance for the next practical fabrication process. While Micro-Electro-Mechanical Systems (MEMS) technique has

become matured enough to fabricate microstructures with large feature size and shallow etching depth, it still encounters great challenge in producing high AR dielectric meta-devices. And the high AR meta-device with excellent fabrication quality is extremely important for realizing high-performance wave manipulations. Therefore, we employ FDTD simulations to systematically evaluate the impact of various structural imperfections (specifically vertical etching depth error and lateral morphology error) on the performance of meta-device.

Regarding vertical depth errors, we note that during the deep silicon etching process, several factors, such as pattern duty cycles and equipment conditions, can result in a final etch depth deviating from the initially designed value. To justify the influence of such issue, we adopt full wave simulations to investigate a series of HWPs and QWPs based on the proposed silicon meta-atoms, which have the same lateral dimensions and different etching depths. Figures 3a and 3b show the calculated PCR spectra of the HWPs and QWPs with the same total thickness ($h_1 + h_2 = 538\ \mu m$) and different etching depth values (different h_1), which exhibits quite sensitive behavior to such error. Combined with the analysis of the transmission properties of meta-atoms, we find that the degradation primarily results from the reduced transmittance due to etching depth error, thereby affecting the PCR of meta-devices (See more details in S5 and S6 of the Supplemental Material).

Subsequently, we analyze how lateral morphology errors affect the performance of HWP and QWP. In our experiments, thick photoresists are often used as masking layers in the deep etching process of high AR dielectric structures to endure extended etching. However, thick photoresists typically contain a higher moisture content, which must be removed through baking before the etching process to prevent "resist popping" effect. This prebake operation will reduce the size of the etched pattern, ultimately leading to lateral morphology errors. Notably, such errors usually cause the etched patterns become smaller than the target design. To evaluate the influence of this issue, we employ FDTD simulations to obtain the PCR of the meta-devices (including HWPs and QWPs) with the same etching depth and different lateral

dimensions (assuming a uniform reduction in length and width), as shown in Figs. 3c and 3d. The results show that reducing the lateral size significantly narrows the working bandwidth of the HWP. While the bandwidth of the QWP remains relatively stable, its spectral response exhibits a blue shift. This performance degradation is primarily due to the significant change in the phase difference $\Delta\phi$ caused by the lateral size reduction, ultimately leading to a decrease in the device's PCR (See more details in S5 and S6 of the Supplemental Material).

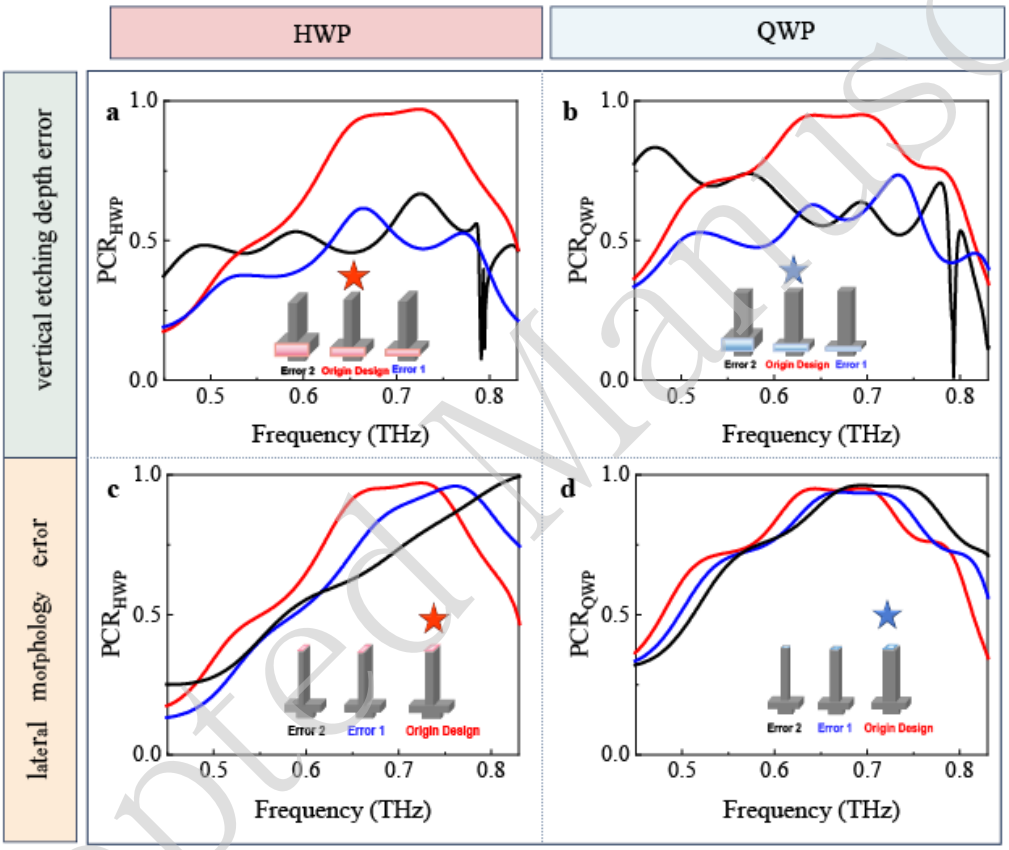

Fig. 3 Impact of structural imperfections on optical performance of the meta-device. a, b Calculated PCR spectra of the HWP and QWP of the original design parameters (red curve) and two different vertical etching depth errors (h_1). In **a** and **b**, the black, blue, and red (original design) cures correspond to h_1 values of 450 μm, 480 μm, and 510 μm in **a** and 450 μm, 480 μm, and 504 μm in **b**. **c, d** Calculated PCR spectra of the HWP and QWP of the original design parameters (red curve) and two different lateral morphology errors (l and w). In **c** and **d**, h_1 is fixed at 480 μm. The black, blue, and red (original design) curves correspond to the (l, w) values of (92.5 μm, 22.5 μm), (96 μm, 26 μm), and (100 μm, 30 μm) in **c**, and (73 μm, 48 μm), (77 μm, 52 μm), and (81 μm, 56 μm) in **d**, respectively. For all simulations, h_3 is fixed at 62 μm.

Experimental fabrication of the silicon meta-devices

Based on our analysis of potential manufacturing errors, we develop an optimized fabrication technique to well address these fabrication challenges and successfully create the high AR silicon meta-devices with high working efficiency across a wide frequency band. All etching operations involve multiple etching and passivation steps during the Bosch process, which is a widely adopted dry etching technique. As illustrated in Fig. 4a, during the passivation step, a polymer layer is deposited to protect the sidewalls of the created microstructures. Next, the polymer at the bottom of the microstructures is rapidly removed to enable the following etching step, while the polymer on the sidewall remains for protecting lateral structures. By precisely controlling the balance between passivation and etching process, it is possible to construct the desired high AR patterns, as shown in Fig. 4b. During the passivation step, a protective polymer layer is deposited on the silicon surface and sidewalls through introducing C_4F_8 at a flow rate of 150 sccm for 2 seconds. This is followed by an auxiliary etching process (Etch 1), which is carried out by introducing SF_6 at the flow rate of 200 sccm and applying a low-frequency (LF) power of 300 W for 1 second. The final step is longitudinal etching (Etch 2), maintaining the SF_6 flow rate at 200 sccm and applying a LF Power of 60 W for 2 seconds. More detailed description of the key fabrication parameters is summarized in Supplemental Table 1.

After that, we transfer the square shaped silicon microstructures (anti-reflection layer) and the backside alignment marks onto a pre-cleaned 600 μm silicon wafer using ultraviolet lithography firstly. The patterned wafer is then etched using an HSE M200 etcher. Subsequently, the high AR pattern is aligned and transferred via backside alignment lithography. The wafer undergoes a second etching process to form the high AR silicon pillar structures. After this process, we thoroughly clean the sample to remove any residual photoresist for subsequent testing. It is worth emphasizing that our optimized preparation process can reduce errors during preparation and also benefit our design engineering applications.

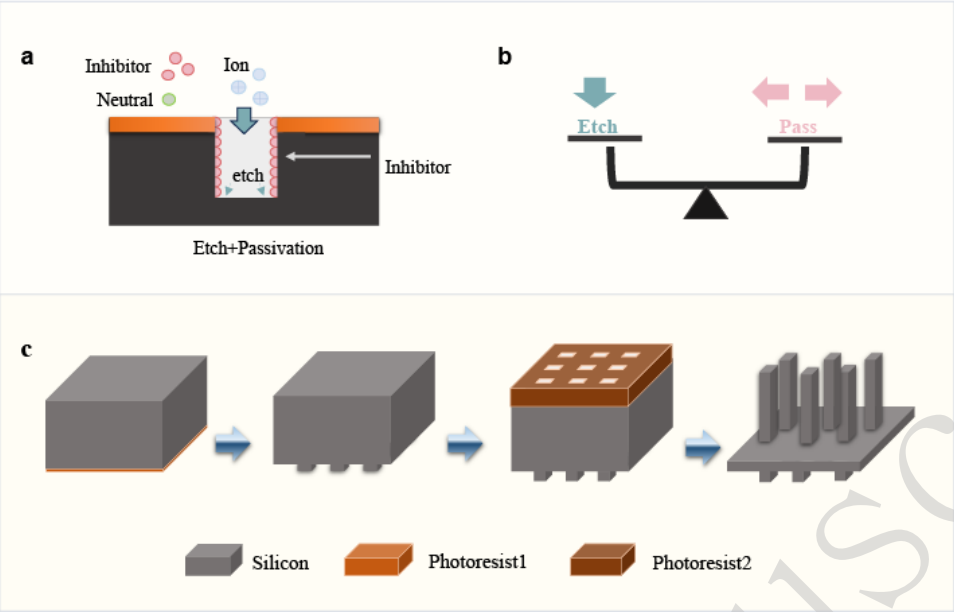

Fig. 4 Deep silicon etching via the Bosch process. **a** High AR anisotropic silicon etching is achieved by the repetitive alternation of etching and passivation steps. **b** The balance between etching and passivation is the key foundation to create high AR microstructures with steep sidewall while avoiding defects such as lateral etching or "black silicon". **c** Flowchart of the fabrication process for our dielectric metasurfaces.

Photoresists are employed as the mask layer throughout all etch processes due to their high pattern resolution, substantial thickness tolerance, and ease of removal. It should be noted that in order to ensure the fabrication accuracy of the pattern, different mask layers need to be employed for various morphologies. For the anti-reflection layer, which requires relatively shallow etching, a thin layer of AZ5214 photoresist was proved to be sufficient for pattern transfer. While the large-feature shallow silicon structures are fabricated, each etching cycle removes approximately 1.03 μm of silicon. Thus, the 62 μm deep anti-reflection layer is successfully etched using about 60 cycles. The fabrication of high AR pillar meta-atoms requires a significantly larger etch depth. During the etching process, because the photoresist mask becomes progressively thinner, a thick resist (e.g., AZ4620) needs to be utilized as the mask layer. Before the deep etching process, the sample needs to be baked for pattern solidification. However, this will introduce a reduction in pattern dimension during fabrication, namely, a pattern shrinkage effect, which should not be overlooked

and will affect the performance of the metasurfaces as analyzed in prior FDTD simulations (see Figs. 3c and 3d). This effect mainly originates from the evaporation of water in the photoresist during the baking process. To compensate for this effect, we intentionally increase the pattern length and width of the pattern during the design stage of mask according to our experience. This strategy effectively mitigates the fabrication-induced lateral deviations, allowing for the precise achievement of the target structural dimensions, as demonstrated in Figs. 5b and 5e. As a result, the repeatability and yield of the optimized fabrication have been significantly improved, effectively meeting the demands for highly robust device preparation.

Additionally, the etching depth is precisely controlled by etch rate and cycle count, which is critical for fabricating high-quality silicon meta-atoms (Figs. 3a and 3b). The etch rate for different pattern duty cycles is determined through the real-time monitoring of the etch depth, as shown in Figs. 5a and 5d. This approach enables precise control over etching depth, thereby minimizing errors induced by vertical non-uniformity. Throughout the etching process, the balance between etching and passivation cycles is carefully maintained, resulting in excellent sidewall verticality of the fabricated structures, as demonstrated in Figs. 5c and 5f.

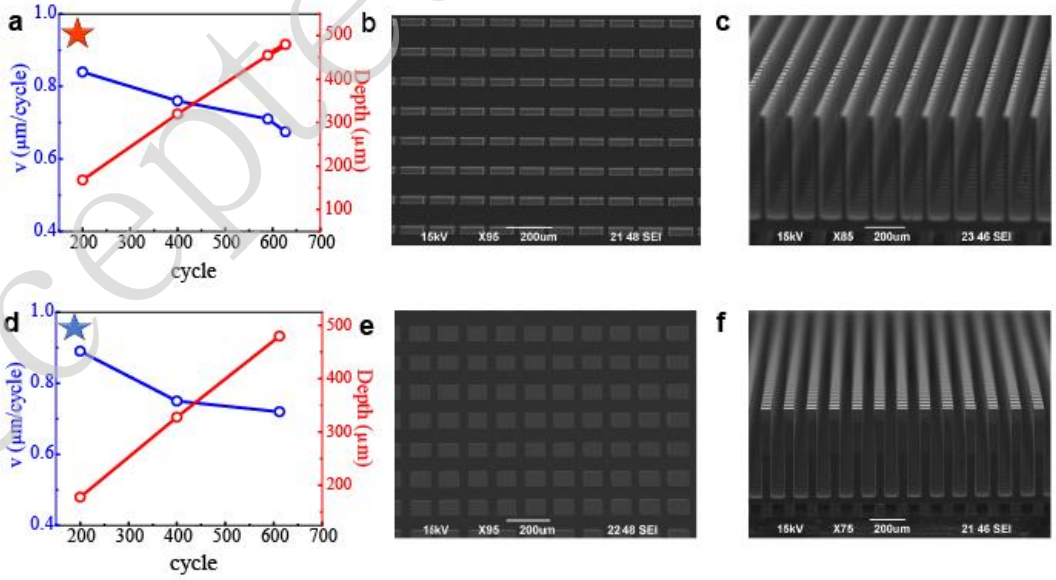

Fig. 5 Key fabrication conditions and scanning electron microscope (SEM) images of samples. **a, d** Etch rates and etching depth versus the cycle number for the high AR layer of HWP and QWP, respectively. Top-view (**b, e**) and side-view (**c,**

f) SEM images of fabricated HWP (**b, c**) and QWP **(e, f)** samples.

Characterization of the fabricated HWP and QWP based on high AR silicon meta-atoms

To demonstrate the proposed design strategy and fabrication methodology, we characterize the polarization conversion performance of the fabricated meta-wave-plate samples based on a THz time-domain spectroscopy (TDS) system. Figures 6a–6c present the simulated and measured transmittance, transmission phase difference between two cross-polarization cases, and the corresponding PCR of the constructed HWP. The reference signal is obtained by replacing the meta-device by the open air and performing the similar measurement. The experimental results, showing excellent agreement with full-wave simulations, demonstrate that the HWP sample shows nearly unity transmittance, the phase difference of about π, and high PCR (PCR > 0.6) over a broad frequency range (0.6–0.8 THz, corresponding to a relative bandwidth of 28.57%). In addition, Figs. 6d–6f show the simulated and measured transmission properties of the fabricated QWP, confirming the high polarization conversion performance (PCR > 0.6) across the target frequency band of 0.5–0.8 THz (relative bandwidth: 46.15%). Overall, the strong consistency between experimental and simulated results validates the effectiveness and reliability of our fabrication strategy in realizing high-performance THz meta-devices based on high AR silicon structures.

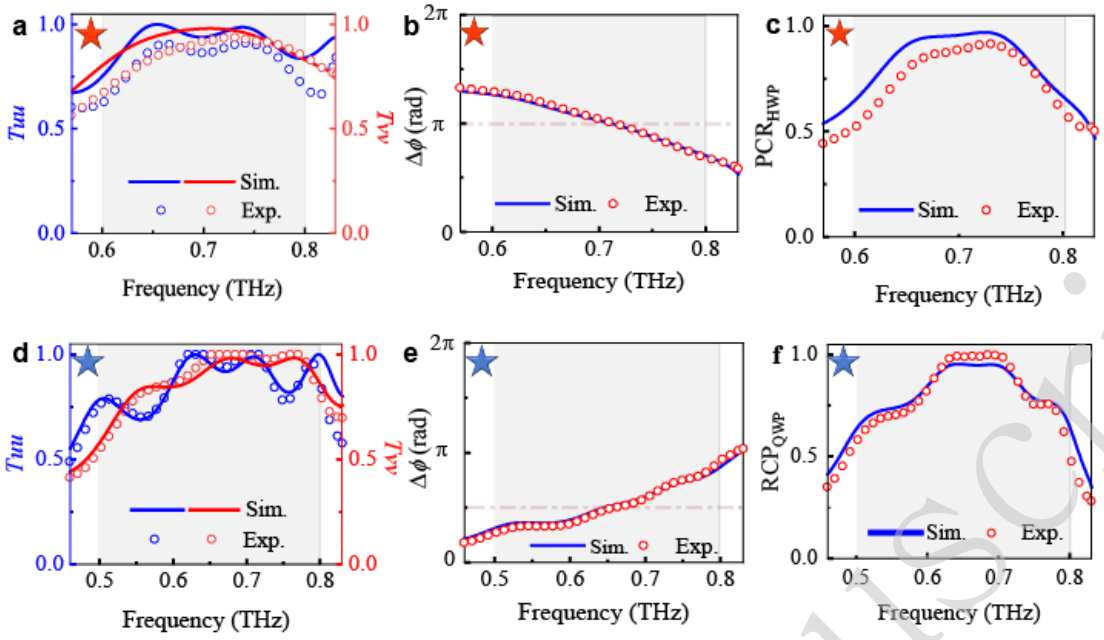

Fig. 6 Optical performance of the fabricated HWP and QWP. a Transmittance efficiency (T_{uu} and T_{vv}), **b** transmittance phase difference ($\Delta\phi$) and **c** PCR of HWP. **d** Transmittance efficiency (T_{uu} and T_{vv}), **e** transmittance phase difference ($\Delta\phi$) and **f** PCR of QWP. Measured data is shown in symbols, while simulation results are represented by solid lines.

Experimental demonstration of the high-efficiency and broadband metalens

The proposed design and fabrication methodology can also be applied to develop various high-efficiency functional meta-devices. For instance, we have designed and fabricated the flat metalens utilizing geometric phase mechanism, as illustrated in Fig. 7a. Based on the designed high-performance HWP as building blocks, we encode the following phase distribution inside the designed PB meta-device for the RCP light illumination case via simply tailoring the orientations of the meta-atoms at each local position:

$$\varphi(x,y) = -k\left(\sqrt{x^2+y^2+F^2}-F\right) \tag{4}$$

where k is the wave vector of the light in free space, (x, y) denotes the position of the meta-atom on the metasurface, and F is the focal length ($F = 5$ mm at the central frequency of 0.7 THz).

The fabricated metalens sample with a total size of 10×10 mm^2 is shown in Figs. 7b and 7c. Using a THz focal plane imaging system (see experimental setup in S7 of

the Supplemental Material), we have measured the different components of the transmitted electric field distributions under the RCP illumination in the frequency range of 0.6–0.8 THz. Based on these data, we can retrieve the electric fields in the *xoz* plane carrying either LCP or RCP components, as presented in Figs. 7d and 7e. Clearly, the incident RCP beam is efficiently converted into LCP one focused in the pre-designed focal plane. Owing to the intrinsic dispersion nature of geometric phase, the focal spot gradually shifts away from the metalens as the frequency increases, corresponding to an increase in focal length and a decrease in NA, as shown in Figs. 7f and 7g.

Figure 7h depicts the measured focusing efficiency of the fabricated metalens, which exceeds 85.56% across the entire operating bandwidth of 0.6–0.8 THz and reaches the highest value of 87% at 0.7 THz. Here, the focusing efficiency is defined as the ratio between the integrated power carried by the focal beam carrying the cross-polarization and that of transmitted THz beam. For comparison, full-wave simulation results show good agreement with experimental measurements (See detailed information in S8 of the Supplemental Material).

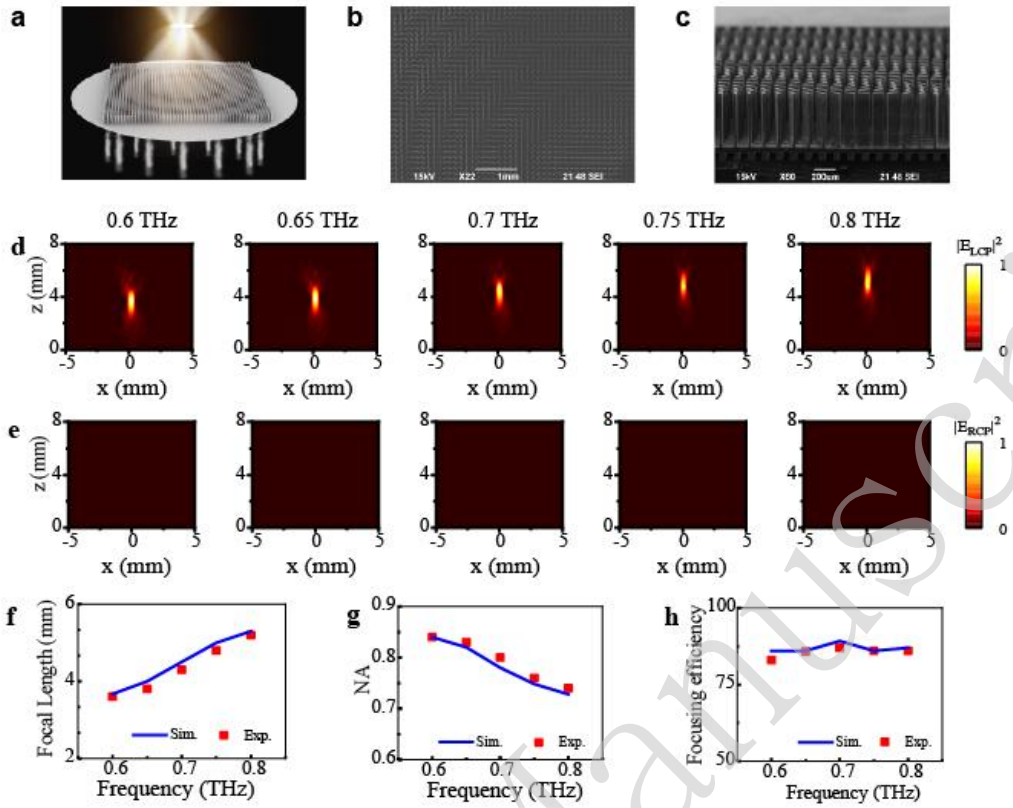

Fig. 7 Experimental characterization of the metalens. **a** Schematic illustration of the metalens. **b, c** Top-view and side-view SEM images of the fabricated sample. **d, e** Measured electric field intensity projected to LCP (**d**) and RCP (**e**) components in the *xoz* plane (y = 0 mm) of the meta-lens under RCP THz wave illumination with different frequencies. **f, g, h** Measured and simulated focal length (**f**), NA (**g**), and focusing efficiency (**h**) of the metalens as a function of frequency.

Discussion and Conclusion

In summary, we have developed an optimized deep etching technique to construct high AR (about 19.2:1) dielectric THz meta-device with a high working efficiency across a wide THz frequency band. By systematically analyzing the influence of potential fabrication errors, we develop an optimized technique to effectively address these critical challenges, enabling the stable fabrication of high-quality silicon meta-device. As proof of concept, we successfully design and fabricate two dielectric meta-devices, i.e., an effective HWP and QWP. Both experimental measurements and full-wave simulations validate the high-efficiency polarization conversion effects across a broad target frequency band. The proposed THz meta-wave-plates exhibit superior comprehensive performances in terms of AR,

absolute PCR and working bandwidth over the previous literatures[57,61-65] (see Supplemental Table 2). Furthermore, by integrating the designed HWP with the concept of geometric phase, we have realized a high-efficiency and broadband THz metalens with an average focusing efficiency exceeding 85.56% in the frequency range of 0.6–0.8 THz. Compared to our previous work[57], the fabrication technique has been significantly optimized, achieving enhanced reproducibility and quality in the production of high AR meta-devices. The meta-devices reported in this work exhibit substantially improved performance and the more diverse functionalities. This work not only demonstrates a viable strategy for the design and fabrication of high-performance THz meta-devices but also provides methodological insights into overcoming fabrication bottlenecks in deep etching technique. The proposed framework can be extended to a wide variety of THz meta-devices, paving the way for future applications in high-efficiency polarization control, THz imaging and sensing, wireless communications, and so on.

Acknowledgments

This work is supported by National Key Research and Development Program of China (Grant Nos. 2020YFA0710100, 2022YFA1404701), National Natural Science Foundation of China (Grant No. 12374344), and China Scholarship Council (202306890039). J.R. acknowledges the National Research Foundation (NRF) grant (RS-2024-00356928) funded by the Ministry of Science and ICT (MSIT) of the Korean government. We acknowledge technical support from Fudan Nanofabrication Laboratory for sample fabrications.

Author details

[1]Shanghai Engineering Research Centre of Ultra Precision Optical Manufacturing, Department of Optical Science and Engineering, College of Future Information Technology, Fudan University, Shanghai, 200433, China

[2]Department of Mechanical Engineering, Pohang University of Science and

Technology (POSTECH), Pohang, 37673, Republic of Korea

[3]Department of Chemical Engineering, Pohang University of Science and Technology (POSTECH), Pohang, 37673, Republic of Korea

[4]Department of Electrical Engineering, Pohang University of Science and Technology (POSTECH), Pohang, 37673, Republic of Korea

[5]POSCO-POSTECH-RIST Convergence Research Center for Flat Optics and Metaphotonics, Pohang, 37673, Republic of Korea

[6]Shanghai Key Laboratory of Metasurfaces for Light Manipulation, Shanghai, 200433, China

[7]Yiwu Research Institute of Fudan University, Chengbei Road, Yiwu City, 322000, China

Authors' contributions

Z.Z. conducted the numerical simulations, fabricated the samples, performed the terahertz experiments, analyzed the results, and made the final manuscript. X.L. developed the theoretical model, conducted the numerical simulations, analyzed the results, and prepared the original draft. S.S. and J.R. initiated the idea and revised the manuscript. All authors participated in the discussion and confirmed the final manuscript.

Conflict of interest

The authors declare that they have no conflict of interest.

References

1. Ferguson, B. & Zhang, X. C. Materials for terahertz science and technology. *Nature Materials* **1**, 26-33 (2002).

2. Zang, X. F. et al. Metasurfaces for manipulating terahertz waves. *Light*: *Advanced Manufacturing* **2**, 10 (2021).

3. Ma, J. J. et al. Security and eavesdropping in terahertz wireless links. *Nature* **563**, 89-93 (2018).

4. Fu, X. J. et al. Terahertz beam steering technologies: from phased arrays to field-programmable metasurfaces. *Advanced Optical Materials* **8**, 1900628 (2020).

5. Lyu, J. M. et al. Review on the terahertz metasensor: from featureless refractive index sensing to molecular identification. *Photonics Research* **12**, 194 (2024).

6. Jin, Z. W. et al. Advances in nanoengineered terahertz technology: generation, modulation, and bio-applications. *Research* **8**, 0562 (2025).

7. Grady, N. K. et al. Terahertz metamaterials for linear polarization conversion and anomalous refraction. *Science* **340**, 1304-1307 (2013).

8. Liu, S. et al. Convolution operations on coding metasurface to reach flexible and continuous controls of terahertz beams. *Advanced Science* **3**, 1600156 (2016).

9. Li, J. T. et al. Dynamic phase assembled terahertz metalens for reversible conversion between linear polarization and arbitrary circular polarization. *Opto-Electronic Advances* **5**, 210062 (2022).

10. Masson, J. B. & Gallot, G. Terahertz achromatic quarter-wave plate. *Optics Letters* **31**, 265-267 (2006).

11. Sen, M. et al. Achromatic terahertz quarter-wave Fresnel rhomb retarder. *Applied Physics Letters* **122**, 241102 (2023).

12. Chen, H. T., Taylor, A. J. & Yu, N. F. A review of metasurfaces: physics and applications. *Reports on Progress in Physics* **79**, 076401 (2016).

13. Su, V. C. et al. Advances in optical metasurfaces: fabrication and applications [Invited]. *Optics Express* **26**, 13148-13182 (2018).

14. Ding, F., Pors, A. & Bozhevolnyi, S. I. Gradient metasurfaces: a review of fundamentals and applications. *Reports on Progress in Physics* **81**, 026401 (2018).

15. Sun, S. L. et al. Electromagnetic metasurfaces: physics and applications. *Advances in Optics and Photonics* **11**, 380-479 (2019).

16. Li, L. L. et al. Intelligent metasurfaces: control, communication and computing. *eLight* **2**, 7 (2022).

17. Yu, N. F. et al. Light propagation with phase discontinuities: generalized laws of reflection and refraction. *Science* **334**, 333-337 (2011).

18. Sun, S. L. et al. Gradient-index meta-surfaces as a bridge linking propagating waves and surface waves. *Nature Materials* **11**, 426-431 (2012).

19. Huang, L. L. et al. Dispersionless phase discontinuities for controlling light propagation. *Nano Letters* **12**, 5750-5755 (2012).

20. Lin, D. M. et al. Dielectric gradient metasurface optical elements. *Science* **345**, 298-302 (2014).

21. Jia, R. D. et al. Achromatic dielectric metasurface with linear phase gradient in the terahertz domain. *Advanced Optical Materials* **9**, 2001403 (2021).

22. He, T. et al. Perfect anomalous reflectors at optical frequencies. *Science Advances* **8**, eabk3381 (2022).

23. Huang, L. L. et al. Helicity dependent directional surface plasmon polariton excitation using a metasurface with interfacial phase discontinuity. *Light*: *Science & Applications* **2**, e70 (2013).

24. Pors, A. et al. Efficient unidirectional polarization-controlled excitation of surface plasmon polaritons. *Light*: *Science & Applications* **3**, e197

(2014).

25. Fang, B. et al. Manipulating guided wave radiation with integrated geometric metasurface. *Nanophotonics* **11**, 1923-1930 (2022).

26. Chen, Y. Z. et al. Efficient meta-couplers squeezing propagating light into on-chip subwavelength devices in a controllable way. *Nano Letters* **23**, 3326-3333 (2023).

27. Zhang, X. Q. et al. Anomalous surface wave launching by handedness phase control. *Advanced Materials* **27**, 7123-7129 (2015).

28. Pan, W. K. et al. High-efficiency generation of far-field spin-polarized wavefronts via designer surface wave metasurfaces. *Nanophotonics* **11**, 2025-2036 (2022).

29. Wang, Z. et al. Efficient generation of vectorial terahertz beams using surface-wave excited metasurfaces. *Opto-Electronic Science* **4**, 240024 (2025).

30. Ding, F. & Bozhevolnyi, S. I. Enriching surface plasmons with metasurfaces. *Photonics Insights* **2**, C02 (2023).

31. Chen, X. Z. et al. Dual-polarity plasmonic metalens for visible light. *Nature Communications* **3**, 1198 (2012).

32. Khorasaninejad, M. et al. Metalenses at visible wavelengths: diffraction-limited focusing and subwavelength resolution imaging. *Science* **352**, 1190-1194 (2016).

33. Wang, S. M. et al. A broadband achromatic metalens in the visible. *Nature Nanotechnology* **13**, 227-232 (2018).

34. Wang, Y. J. et al. High-efficiency broadband achromatic metalens for near-IR biological imaging window. *Nature Communications* **12**, 5560 (2021).

35. Kim, J. et al. Large‐area floating display with wafer‐scale manufactured metalens arrays. *Laser & Photonics Reviews* **19**, 2401425 (2025).

36. Huang, L. L., Zhang, S. & Zentgraf, T. Metasurface holography: from fundamentals to applications. *Nanophotonics* **7**, 1169-1190 (2018).

37. Deng, Z. L. et al. Diatomic metasurface for vectorial holography. *Nano Letters* **18**, 2885-2892 (2018).

38. Zhao, R. Z. et al. Multichannel vectorial holographic display and encryption. *Light*: *Science & Applications* **7**, 95 (2018).

39. Wang, H. et al. Metasurface with dynamic chiral meta-atoms for spin multiplexing hologram and low observable reflection. *Photonix* **3**, 10 (2022).

40. Shi, Y. Y. et al. Augmented reality enabled by on‐chip meta‐holography multiplexing. *Laser & Photonics Reviews* **16**, 2100638 (2022).

41. Yu, Z. P. et al. Spin-orbit-locking vectorial metasurface holography. *Advanced Materials* **37**, 2415142 (2025).

42. Meng, W. J. et al. Ultranarrow-linewidth wavelength-vortex metasurface holography. *Science Advances* **11**, eadt9159 (2025).

43. Zhan, Q. W. Cylindrical vector beams: from mathematical concepts to applications. *Advances in Optics and Photonics* **1**, 1-57 (2009).

44. Pu, M. B. et al. Catenary optics for achromatic generation of perfect optical angular momentum. *Science Advances* **1**, e1500396 (2015).

45. Shen, Y. J. et al. Optical vortices 30 years on: OAM manipulation from topological charge to multiple singularities. *Light*: *Science & Applications* **8**, 90 (2019).

46. Bao, Y. J., Ni, J. C. & Qiu, C. W. A minimalist single-layer metasurface for arbitrary and full control of vector vortex beams. *Advanced Materials* **32**, 1905659 (2020).

47. Wang, D. Y. et al. Efficient generation of complex vectorial optical fields with metasurfaces. *Light*: *Science & Applications* **10**, 67 (2021).

48. Khurgin, J. B. How to deal with the loss in plasmonics and metamaterials. *Nature Nanotechnology* **10**, 2-6 (2015).

49. Rubin, N. A. et al. Matrix Fourier optics enables a compact full-Stokes polarization camera. *Science* **365**, eaax1839 (2019).

50. Koshelev, K. & Kivshar, Y. Dielectric resonant metaphotonics. *ACS Photonics* **8**, 102-112 (2021).

51. Hu, Y. Q. et al. All-dielectric metasurfaces for polarization manipulation: principles and emerging applications. *Nanophotonics* **9**, 3755-3780 (2020).

52. Yang, W. H. et al. Advanced manufacturing of dielectric meta-devices. *Photonics Insights* **3**, R04 (2024).

53. Álvarez-Sanchis, J. A. et al. Loss-induced performance limits of all-dielectric metasurfaces for terahertz sensing. *Physical Review Applied* **19**, 014009 (2023).

54. Choi, M. et al. Realization of high-performance optical metasurfaces over a large area: a review from a design perspective. *npj Nanophotonics* **1**, 31 (2024).

55. Wang, Z. et al. Bifunctional manipulation of terahertz waves with high-efficiency transmissive dielectric metasurfaces. *Advanced Science* **10**, 2205499 (2023).

56. Xu, Y. et al. Broadband achromatic terahertz metalens constituted by

Si–SiO_2–Si hybrid meta‐atoms. *Advanced Functional Materials* **33**, 2302821 (2023).

57. Yao, Y. et al. High-aspect-ratio silicon metasurfaces: design, fabrication, and characterization. *Applied Sciences* **13**, 9607 (2023).

58. Wu, B. et al. High aspect ratio silicon etch: a review. *Journal of Applied Physics* **108**, 051101 (2010).

59. Zhang, H. F. et al. High-efficiency dielectric metasurfaces for polarization-dependent terahertz wavefront manipulation. *Advanced Optical Materials* **6**, 1700773 (2018).

60. Zheng, C. L. et al. Creating longitudinally varying vector vortex beams with an all-dielectric metasurface. *Laser & Photonics Reviews* **16**, 2200236 (2022).

61. Zhang, Z., Gong, Y. D. & Pang, K. Optimization and design on multi-layers of dielectric metasurface as broadband terahertz quarter wave plate. *Journal of Optics* **24**, 105101 (2022).

62. Xing, X. H. et al. An all-silicon design of a high-efficiency broadband transmissive terahertz polarization convertor. *Frontiers of Optoelectronics* **16**, 40 (2023).

63. Zi, J. C. et al. Antireflection-assisted all-dielectric terahertz metamaterial polarization converter. *Applied Physics Letters* **113**, 101104 (2018).

64. Zi, J. C. et al. Terahertz polarization converter based on all-dielectric high birefringence metamaterial with elliptical air holes. *Optics Communications* **416**, 130-136 (2018).

65. Wang, D. C. et al. Complete terahertz polarization control with broadened bandwidth via dielectric metasurfaces. *Nanoscale Research Letters* **16**, 157 (2021).